AGU PUBLICATIONS

JGR

Journal of Geophysical Research: Solid Earth

RESEARCH ARTICLE
10.1002/2017JB014240

Key Points:
- In Situ micropillar compression experiments applied to the fine-grained porous clay matrix in shales
- Mechanical anisotropy of shales at different length scales
- Anisotropic failure mechanism in shales

Correspondence to:
L. M. Keller,
kelu@zhaw.ch

Citation:
Keller, L. M., J. J. Schwiedrzik, P. Gasser, and J. Michler (2017), Understanding anisotropic mechanical properties of shales at different length scales: In situ micropillar compression combined with finite element calculations, *J. Geophys. Res. Solid Earth*, *122*, doi:10.1002/2017JB014240.

Received 24 MAR 2017
Accepted 9 JUN 2017
Accepted article online 10 JUN 2017

Understanding anisotropic mechanical properties of shales at different length scales: In situ micropillar compression combined with finite element calculations

Lukas M. Keller[1], Jakob J. Schwiedrzik[2], Philippe Gasser[3], and Johann Michler[2]

[1]ZHAW, University of Applied Sciences, Zurich, Switzerland, [2]Laboratory of Mechanics of Materials and Nanostructures, EMPA, Swiss Federal Laboratories for Material Science and Technology, Thun, Switzerland, [3]ScopeM, Scientific Center for Optical and Electron Microscopy, ETHZ, Swiss Federal Institute of Technology, Zurich, Switzerland

Abstract From microstructural observations and experimental work it is known that shales consist of a mechanically weak porous fine-grained clay matrix with embedded and mechanically strong silt/sand grains. Thereby, the respective contents of weak and strong constituents control bulk mechanical properties. In addition, the clay matrix is characterized by a preferred orientation of clay platelets, which are a major control on the bulk anisotropy of shales. To date, little is known about the micromechanical properties of the fine-grained porous clay matrix, which is particularly true in case of its micromechanical anisotropy. Such information can, however, only be assessed on the microscale. Therefore, the drained micromechanical properties parallel and perpendicular to bedding were investigated by means of compressing micropillars with a flat punch indenter in a scanning electron microscope. Microscopic failure mechanism was found to be anisotropic: (i) in case loading was parallel to bedding it occurred by a combination of localized shearing, kinking/buckling of elongated clay aggregates, and bedding parallel splitting and (ii) for loading perpendicular to bedding failure occurred mainly by localized shearing. The measured stiffness of the drained porous clay matrix perpendicular (E_v) and parallel (E_h) to bedding was about 8 GPa and 30 GPa, respectively. Using these stiffness values as input in voxel-based finite element modeling and in combination with realistic microstructures, which are characterized with different contents of "soft" and "hard" constituents, revealed that the measured high microscale anisotropy $E_h/E_v = 3.75$ is crucial in understanding the bulk anisotropy of clay rocks.

1. Introduction

From the disposal of nuclear waste over the exploitation of gas to CO_2 sequestration, clay rocks/shales are of fundamental importance and consequently, a deeper understanding of its mechanical properties became increasingly important during recent years. Here the focus is on the Opalinus Clay unit, which is considered as potential host rock for nuclear waste in Switzerland [*Nagra,* 2002, 2004; *Andra,* 2005]. Opalinus Clay is a multiphase, anisotropic, and compositionally diverse material, which exhibits different structural features on multiple length scales. In addition, this sedimentary rock formation varies in the relative contents of clay and nonclayey mineral grains, which affects petrophysical properties.

Clay rocks are often considered as a binary mixture of a porous clay matrix and nonclayey mineral grains. This simplification was made in terms of permeability [*Revil and Cathles,* 1999] and solute diffusion [*Robinet et al.,* 2012; *Keller et al.,* 2015] and also in terms of elastic properties [e.g., *Sone and Zoback,* 2013]. In the latter case the clay matrix was considered as the "soft" and nonclayey minerals as the "stiff" end-members, respectively. Making use of such mixture models to predict mechanical properties requires the knowledge and understanding of mechanical properties related to the respective homogenous constituents. The elastic properties of nonclayey minerals such as carbonates and quartz are well known; on the contrary, the elastic properties of the fine-grained clay matrix are largely unknown.

Regarding micromechanical models of shales, the bulk anisotropy is often considered by a combination of textural-related anisotropy and pore-induced anisotropy, whereas pores are considered as oblate spheroids with a shape-preferred orientation [*Sarout and Gueguen,* 2008]. The predictive capabilities of such a model depend on the calibration of the model parameters such as the anisotropy that can be attributed to the preferred orientation of platy clay minerals and/or the aspect ratio of pores and its orientation distribution. Using realistic pore microstructures in combination with finite element modeling to predict the elastic

behavior of shales reduces the number of unknown parameters. But also in this approach, the mechanical properties of the porous solid clay matrix must be known [*Arns et al.,* 2002*; Keller,* 2016]. Microstructural investigations on multiple length scales provide the information on the spatial distribution of the constituents, which is crucial for the prediction of the mechanical properties. But in order to use this multiscale information, the mechanical response of the respective homogenous constituents must be known. This in particular concerns the fine-grained porous clay matrix, of which properties are controlled at the nanoscale to micron scale. With an understanding of shales as a multiphase and multiscale material, the micron-scale mechanical behavior of the different shale constituents is of particular interest.

Recent instrumental developments allow the measurement of the uniaxial mechanical behavior at the micrometer scale by means of micropillar compression [*Michler et al.,* 2007*; Maeder et al.,* 2011*; Schwiedrzik et al.,* 2014]. Regarding shales, nanoindentation experiments have been performed by *Ulm and Abousleiman* [2006]. These workers confirmed that particle-to-particle contact and characteristic packing densities control the nanogranular properties of shales. *Bobko and Ulm* [2008] also applied nanoindentation experiments to shales and found that nanomechanical building blocks behave transverse isotropic in stiffness and isotropic in strength. *Veytskin et al.* [2017] combined nanoindentation experiments with energy-dispersive X-ray spectrometry, which allowed determining nanoindentation mechanical properties and the local mineralogy. *Abousleiman et al.* [2016] applied micropillar compression testing and microcantilevers testing to a kerogen-rich shale to investigate the micromechanical properties. However, during the latter work only one out of the three prepared micropillars was successfully loaded to failure. Hence, little is known on the micromechanical behavior of shales under uniaxial compression, not to mention the almost complete lack of knowledge regarding the micromechanical anisotropy of the fine-grained clay matrix in shales.

So far, mainly nanoindenation experiments were applied to shales in order to investigate its micromechanical properties. Here we compressed micropillars with an in situ scanning electron microscope (SEM) indenter with the aim to determine the micromechanical properties of the fine-grained porous clay matrix in Opalinus Clay. This approach was chosen because the mechanical properties of fine-grained porous clay matrix are controlled on the microscale. Thereby, vertical and horizontal stiffness and uniaxial anisotropic compression strength of the porous clay matrix were determined on the micrometer length scale. These micromechanical quantities can be compared with the respective values determined on the macroscale. In addition, the determined values allowed an approximation of the transverse isotropic stiffness matrix related to the porous clay matrix, which can be used in combination with voxel-based finite element modeling in order to gain insight into linear elastic behavior on mesoscale (millimeter scale).

2. Experimental Procedure

The starting point of this investigation is a drill core labeled BGC-1 (depth 3.2 m), which was extracted from the Mont Terri underground rock laboratory, Switzerland. From this core, clay cubes with edge lengths of about 3 mm were prepared using a high-precision diamond saw. Micromechanical compression tests require flat and damage-free surfaces, and therefore, the raw cube surfaces were polished under high vacuum using a broad ion beam (BIB)-polishing machine. One surface parallel and one surface perpendicular to bedding were ion polished for 2 h (Figure 1). Sample preparation under high vacuum increases the evaporation of water significantly, and no outgassing was observed after the polishing step in the scanning electron microscope during micropillar preparation. Therefore, the pore space is expected to be devoid of water and the determined mechanical properties are considered as those of the drained fine-grained porous clay matrix.

Then, the samples were transferred into a FIB-SEM instrument (scanning electron microscopy with a focused ion beam) and the polished surfaces were imaged and the localities of the future micropillars were selected.

Drying cracks oriented parallel to bedding, and visible on the surface oriented perpendicular to bedding, were carefully excluded as sample locations (Figure 1b). Note that the avoidance of these visible cracks may lead to a selection of stronger sample material, as cracks on this scale cannot be avoided in larger-scale samples (see section 4). Then, clay matrix micropillars were prepared using the FIB technique. Four pillars in each direction (e.g., parallel and perpendicular to bedding) were prepared. All eight manufactured micropillars were prepared within the intact fine-grained clay matrix (Figures 1c and 1d) and had a diameter of about 10 μm and height of about 20 μm. Exact measurements of each micropillar (diameter and height) were obtained in situ in order to compute the stress and strain from the corrected load-displacement curve.

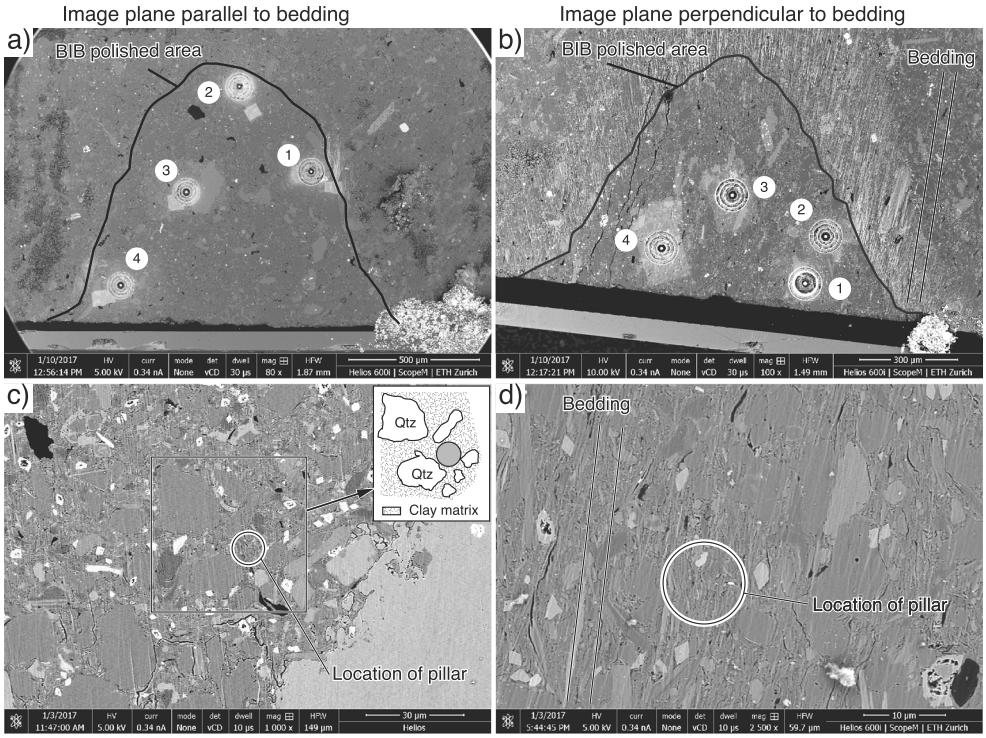

Figure 1. Overview (a and b) BSE images showing the pillar locations and (c and d) high-resolution BSE images showing selected locations for future pillar preparation within the fine-grained clay matrix. Figure 1a shows image plane and polished area parallel to bedding. Figure 1b shows image plane and polished area perpendicular to bedding. Figure 1c shows location of future pillar 3 that was prepared in the area that is parallel to bedding. Figure 1d shows location of future pillar 3 that was prepared in the area that is perpendicular to bedding.

Regarding the small sample size, the existence of spatial microstructural heterogeneities may lead to uncertainties in the determined micromechanical properties. This problem is related to the concept of the representative volume element (RVE) of the elastic properties. *Keller* [2016] quantified this type of uncertainties of the elastic properties related to the solid porous framework of the clay matrix using reconstructed pore microstructures of Opalinus Clay in combination with voxel-based finite element modeling. The uncertainties/RVE were calculated using a statistical analysis [*Kanit et al.,* 2003]. It turned out that for a sample size with an edge length of 1 μm, the relative error on the Voigt-Reuss-Hill average bulk modulus is around 10%. This uncertainty is related to a single realization. Increasing the number of realizations reduces the uncertainties. This analysis implies that the uncertainties induced by spatial variation of the pore microstructure for a sample of the size of the micropillars can be neglected. However, apart from the spatial variation of the pore microstructure, the spatial variation in the arrangement of the minerals contributes also to the uncertainties, which in particular concerns the presence of nonclay minerals of clay particle size. This problem was addressed by performing several measurements, which reduces the uncertainties. It turned out that the relative error on the determined mean value of the Young's moduli ranges up to about 14%, which was accepted here (see below).

Micropillars were compressed inside a FIB-SEM workstation (Tescan Lyra, Czech Republic) using an in situ indenter (Alemnis AG, Switzerland) equipped with a diamond flat punch tip, and force and tip displacement were recorded simultaneously [*Wheeler et al.,* 2013]. Compression was carried out in displacement control at a speed of 20 nm/s. Pillars were compressed to failure with two intermittent partial unloading cycles to measure the apparent unloading modulus at 250 nm and 500 nm displacement. Force displacement data were corrected for frame compliance and elastic micropillar sink in using the modified Sneddon approach [*Zhang et al.,* 2006] and subsequently converted to true stress-strain data using the known micropillar dimensions and the assumption of plastic incompressibility [*Ashby* and *Jones*, 1980]. Compressive strength was defined as the maximum stress in the true stress-strain curve, and the elastic modulus was measured by a linear fit to

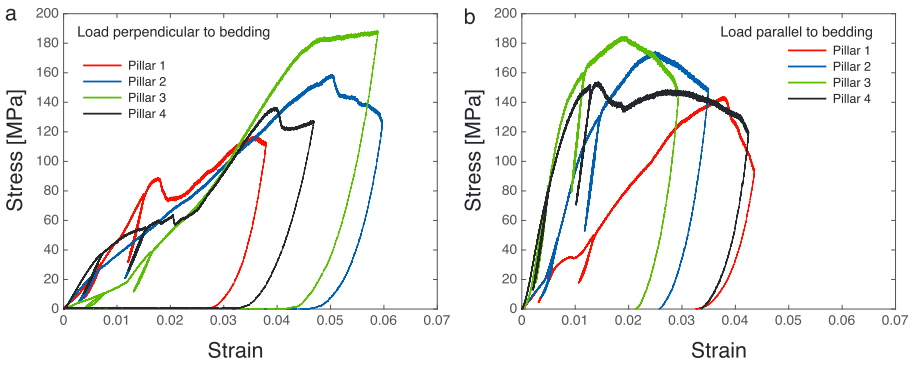

Figure 2. Compressive stress-strain curves of micropillars for load (a) perpendicular and (b) parallel to bedding.

the second partial unloading cycle. Two compression experiments showed stiffness values (Pillar 1 in Figures 2a and 2b), which deviated more than 50% from the other three curves and were thus excluded from the calculation of the mean micromechanical properties. These discrepancies can be attributed to the fact that it is impossible to reach perfect parallelism between the top of the pillar and the indenter flat punch tip [*Soler et al.,* 2012]. Imperfect parallelism can induce stress concentration at the initial contact point of the micropillar, which leads to early plastification and the apparent reduction of the initial loading stiffness [*Soler et al.,* 2014].

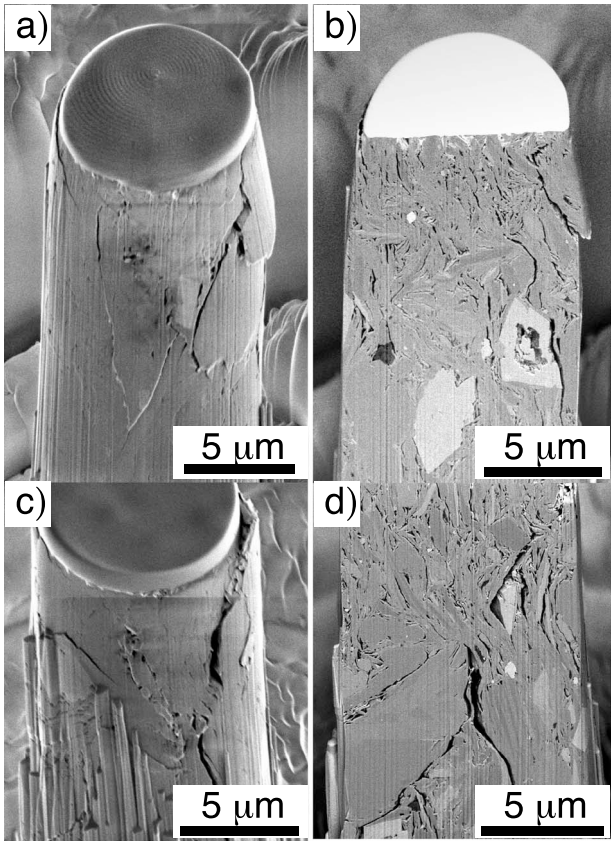

Figure 3. Compilation of images showing micropillars after failure in case the load was applied parallel to bedding. (a and c) SE images showing the whole pillars. (b and d) BSE images showing a cross section through the respective pillar. Orientation of the bedding plane is vertical. Note (i) that the clay platelets tend to be vertical oriented and (ii) that failure is associated with the formation of multiple zones of localized shear deformation, kinking, and axial splitting fractures.

3. Experimental Results

In case the load was applied perpendicular to bedding, the micropillars showed a quasi-linear response up to yielding, which in some instances was followed by a peak, some plasticity, and finally by strain softening (Figure 2a).

Some pillars showed apparent yielding at an early stage of deformation, which was probably caused by local inhomogeneities, surface roughness, or slight misalignment of the tip and the micropillar top surface. Regarding loading parallel to bedding, the quasi-linear part is followed by some hardening and then by strain softening (Figure 2b). In general, this behavior is characteristic of quasi-brittle materials, which form microcracks after yielding. The global softening behavior is in line with the observed cracked microstructure and the formation of localized shear zones in the micropillars. It is noteworthy that while the measured moduli were highly anisotropic, the ultimate stress showed much smaller differences between the

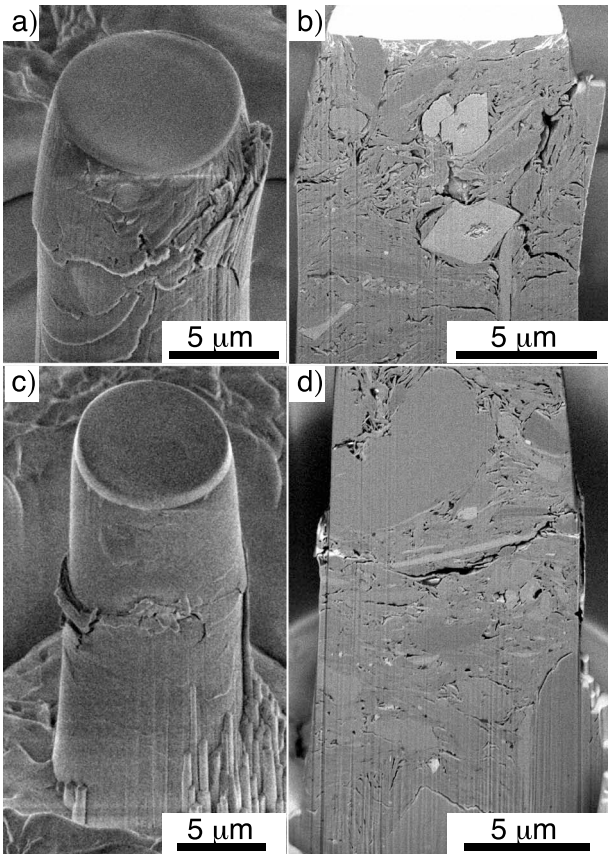

Figure 4. Compilation of images showing micropillars after failure in case the load was applied perpendicular to bedding. (a and c) SE images showing the whole pillars. (b and d) BSE images showing a cross section through the respective pillar. Note that the deformation was accommodated mainly by formation of zones of localized shear deformation. Orientation of the bedding plane is horizontal.

two directions. This is in line with micropillar compression results for other quasi-brittle materials such as bones [*Schwiedrzik et al.,* 2014]. This behavior is also in agreement with results obtained from nanoindentation experiments [*Bobko and Ulm*, 2008]. However, the porous clay matrix behaves more rigid in case a load is applied parallel to bedding when compared to loading perpendicular to bedding (Figure 2). As an example, the applied stress parallel to bedding reaches a mean value of around 128 MPa at 1% vertical strain in contrast to around 36 MPa in case the load is applied perpendicular to bedding. Furthermore, the plasticity is higher in case the load is applied perpendicular to bedding where the clay matrix accommodates a vertical strain of more than 4%.

The mean microscopic strength for uniaxial compression perpendicular to bedding is about 161.4 MPa (e_a = 30.1 MPa), and the one for compression parallel to bedding is about 171.1 MPa (e_a = 17.9 MPa). Regarding the Young's moduli, the experiments yielded mean values of about 8.4 GPa (e_a = 0.6 GPa) (= E_v) in case the load was applied perpendicular to bedding and of 30.2 GPa (e_a = 4.4 GPa) (= E_h) in case the load was applied parallel to bedding. To calculate the absolute error on the mean value of a certain micromechanical property, we used the relation $e_a = 2\mathrm{SD}/\sqrt{n}$, where SD is the standard deviation and n (= 3) is the number of realizations.

In order to gain knowledge on the microscopic failure mechanism, cross sections through the pillars were prepared by FIB, which were then imaged in the SEM (Figures 3 and 4). The preferred orientation of clay platelets or clay aggregates, which defines the bedding plane, can easily be seen. Thereby, the preferred orientation of clay platelets or particles is either parallel or perpendicular to the loading direction. As expected, deviations from the dominant orientation can also be observed. Apparently, failure occurs mainly along grain boundaries between clay particles and along phase boundaries between nonclayey minerals and clay particles. In case the load is applied parallel to bedding, failure leads to the formation of zones of localized shear deformation and cracks, kinking, as well as axial splitting fractures with the dominant fracture orientation being near parallel to bedding (Figures 3 and 5). Occasionally, failure along grain/phase boundaries and associated fracturing occurs in combination with shearing (Figure 5). Shear band formation and axial splitting are common in micropillar compression on brittle crystals [*Howie et al.,* 2012].

Fracturing is limited to the development of single fractures in case load is applied perpendicular to bedding (Figure 4). In this case, shearing initiates within aggregates of clay platelets, of which orientations are close to the orientation of maximum shear stress (Figures 4a and 4b). Hence, local deviation from the crystallographic and/or shape-preferred orientation can initiate shearing in cases where the bedding plane is perpendicular to the direction of principle stress. The anisotropy of failure mechanisms has been also observed in other

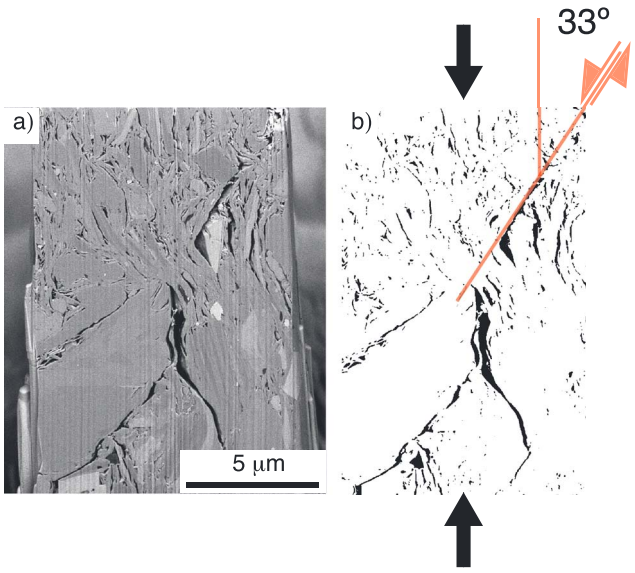

Figure 5. Image showing the failure mechanism in case the load is applied parallel to bedding. Note that the formation of multiple fracturing parallel to bedding is associated with local shearing. The angle between the direction of principle stress and the shear plane is around 30°.

quasi-brittle materials like bone, which showed shear cracking and axial splitting when tested along the fiber direction and shear cracking only when tested perpendicular to the fibers [*Schwiedrzik et al.,* 2014].

4. Discussion

The observed micromechanical behavior of the fine-grained porous clay matrix shall be compared to the corresponding macromechanical properties of the Opalinus Clay. From the qualitative point of view, the anisotropic mechanical behavior on the microscale and macroscale was found to be identical. Uniaxial compressive strength parallel to bedding is slightly higher (i.e., factor 1.15) when compared to compression strength perpendicular to bedding. This relationship is in agreement with macroscopic behavior, but microscopic strength is substantially higher when compared to macroscopic strength. According to the data compilation of *Giger and Marschall* [2014], the values of macroscopic uniaxial compressive strength range up to 40 MPa. Hence, the observed microscopic strength of the porous clay matrix is higher by a factor of around 3 to 4 when compared to macroscopic strength. This difference may be in part related to differences in sample size. It is often observed in material testing that smaller samples are characterized by a higher compressive strength when compared to larger samples. Among others this relationship is reported for glasses [*Griffith,* 1921], bones [*Schwiedrzik et al.,* 2014], and concrete [e.g., *Del Viso et al.,* 2008]. The smaller the sample, the smaller the flaws that it can contain. As the fracture strength in a brittle solid is related to the maximum flaw size, this means that the failure stress of microscale samples will be higher than the macroscopic ones. The lower strength related to larger samples therefore may be explained by the combination of size effect due to internal defect size with the presence of additional stress concentrators like pores, preexisting cracks, or other defects, which would lead to a decrease in failure stress when compared to smaller samples. For smaller samples, which, in addition, were selected under high optical magnification (see above), it is less likely to contain preexisting cracks or other defects. Clay rock core samples are particularly susceptible to development of cracks or other defects because of drilling-induced core fracturing, stress release under atmospheric conditions, and dehydration. Another reason for the higher microscale strength is that the samples were compressed in a drained or dry state. On the macroscale there is little correlation between uniaxial compressive strength and water content [*Giger and Marschall,* 2014]. Hence, it is rather the small sample size than the saturation state, which caused the higher microscale strength. However, given the prominence of interface failures in the deformation behavior of the micropillars, the dependence of microscale uniaxial compressive strength on water content cannot be excluded and remains an open question.

The determined stiffness values are considered as drained microelastic properties of the porous fine-grained clay matrix (see above). E_v accounts for stiffness perpendicular to bedding, and the obtained experimental value of 8.4 ± 0.5 GPa is in excellent agreement with the results obtained by *Keller* [2016]. This work predicted elastic properties of the porous clay matrix as function of porosity using reconstructed pore microstructures in combination with voxel-based finite element modeling. This type of calculation requires the knowledge of the elastic properties of porous solid skeleton, which were estimated using Thomson's anisotropy parameters reported by *Wenk et al.* [2008] in combination with realistic rock densities and *S* and *P* wave velocities. Then, for the expected drainable porosity of 10 vol % the calculation yielded a drained E_v of about 7.5 GPa. Regarding the stiffness parallel to bedding E_h, the micropillar compression tests yielded a value of

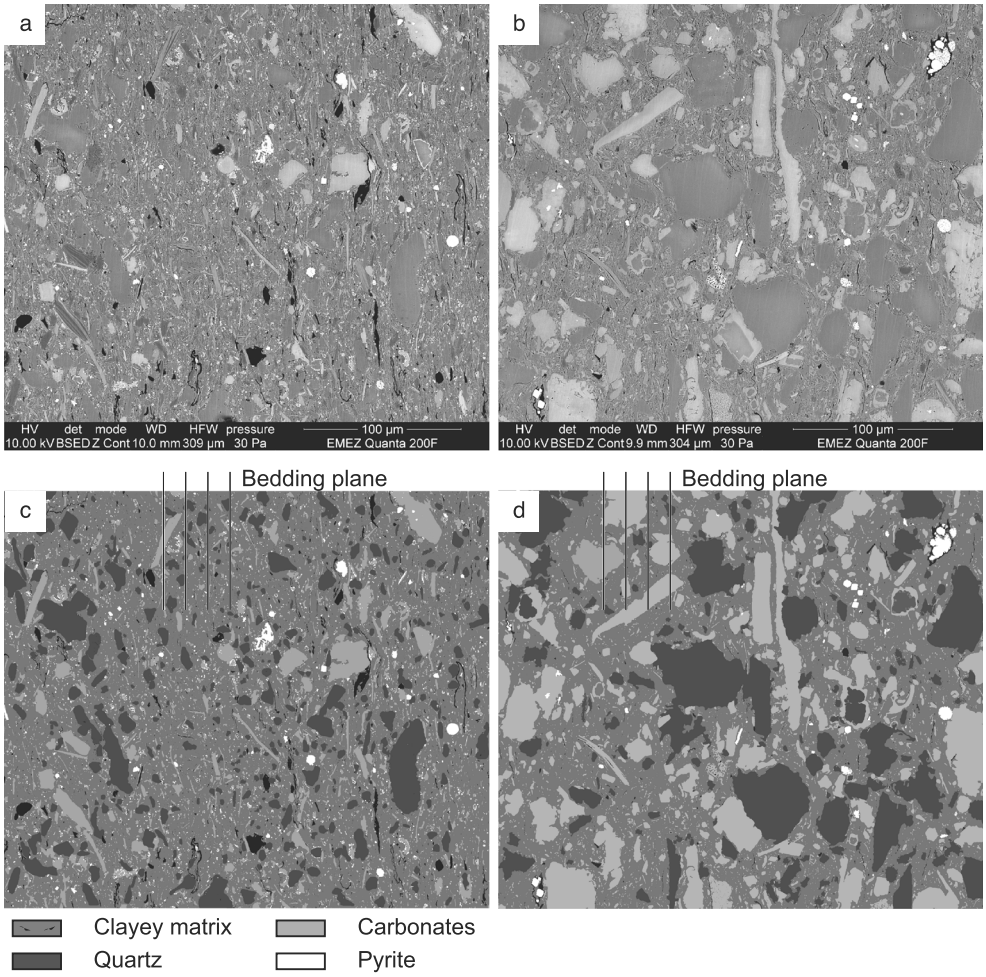

Figure 6. (a and b) Backscatter electron image showing microstructures of clay rocks with different contents of clay matrix. (c and d) The BSE images were segmented, which were then used as input for FEM simulations. Note that the image plane is perpendicular to bedding.

30.2 ± 3.8 GPa, whereas the prediction of *Keller* [2016] yielded around 15 GPa. This suggests that *Keller* [2016] underestimated the microscale anisotropy (i.e., epsilon parameter) related to the solid skeleton.

By reviewing the available experimental work on Opalinus Clay, a considerable spread in the stiffness data is clearly recognizable. Experimentally derived values for drained stiffness perpendicular to bedding range between a few GPa and about 7 GPa [*Giger and Marschall*, 2014]. Experimentally derived values for drained stiffness parallel to bedding are not available, but values of undrained stiffness parallel to bedding range between around 7 and 20 GPa. Thereby, a higher stiffness is indicated for higher confining pressures (i.e., burial depths). Nevertheless, microscale stiffness appears to be higher when compared to macroscale stiffness. As in case of uniaxial compressive strength, the reason for these differences may be related to the large differences in sample size. The presence of porosity, cracks, and other defects influences the mechanical properties [*Walsh*, 1965] and in particular will reduce stiffness [*Keller*, 2016]. As it is was outlined above, in larger samples there is higher probability for the presence of preexisting cracks when compared to small samples, which would lead to higher stiffness in smaller samples.

In the remaining part of this discussion we demonstrate how the determined stiffness values can be used in an upscaling procedure for elastic properties. The aim is to calculate the elastic properties on the hundreds of micrometers length scale by using realistic shale microstructures (Figure 6) in combination with image-based finite element modeling (*Garboczi* [1998] and *Madadi et al.* [2009] for an overview). In order to calculate elastic properties on the hundreds of microns length scale, the elastic moduli of major constituents (clay matrix,

Table 1. Elastic Properties Used for FEM Simulations

	Bulk Modulus (GPa)	Shear Modulus (GPa)	E_h (GPa)	E_v (GPa)	G_{hh} (GPa)	G_{hv} (GPa)	ν_{hh} (GPa)	ν_{hv} (GPa)	ν_{vh} (GPa)
Clay matrix	10.4[a]	-	30.2[b]	8.4[b]	12.0[a]	5.9[a]	0.26[c]	0.33[c]	0.09[a]
Calcite[d]	63.7	31.7							
Quartz[d]	37.9	44.3							
Pyrite[d]	138.6	109.8							

[a]Approximated this study (see text).
[b]Experiments this study.
[c]*Keller* [2016].
[d]*Mavko et al.* [2009].

carbonates, quartz, and pyrite) must be defined (Table 1). An isotropic elastic behavior was assumed for carbonates, quartz, and pyrite. In case of the porous clay matrix we assumed a transverse isotropic behavior. Then, the components of the transverse isotropic compliance tensor **S** can be estimated by using the experimentally determined stiffness values (Table 1) in combination with assumptions on the Poisson's ratios. ν_{hv} and ν_{hh} were set to 0.33 and 0.26, which corresponds to the drained Poisson's ratios proposed by *Keller* [2016] at a drainable porosity of 10 vol % (see above). Thermodynamic rules require that for an elastic material, the compliance tensor **S** must be symmetric [*Love*, 1927] and therefore we have $\nu_{hv} E_v = \nu_{vh} E_h$, which yielded a value of $\nu_{vh} = 0.09$. Furthermore, G_{hh} is dependent on E_h and ν_{hh} and because the bedding plane is considered as a plane of symmetry, we used the relations $G_{hh} = E_h/[2(1 + \nu_{hh})]$. Furthermore, we follow *Naumann and Plischke* [2005] and used the relation $G_{hv} = 1/[1/E_h + 1/E_v + 2\nu_{hh}/E_h]$ (Table 1). Then, all the elastic components in **S** can be calculated by using the usual relations for transverse isotropic materials. Based on the known **S**, an averaged bulk modulus of the porous clay matrix can be calculated by using the Voigt-Reuss-Hill approximation, which yielded a value of about 10.4 GPa. Values of elastic properties related to the solid clay matrix have been experimentally determined by *Vanorio et al.* [2003], who obtained values for the bulk modulus ranging between 6 and 12 GPa. The approximated value falls in the range of experimentally derived values and hence is reasonable.

Then a voxel-based finite element method (FEM) implementation was used to calculate the elastic properties (*Garboczi* [1998] and *Keller* [2016] for more details). The aim is to calculate the effect of nonclayey minerals on the bulk elastic properties. This requires microstructures with different clay matrix contents. Here we used microstructures that are related to samples from the Schlattingen SLA-1 borehole, Switzerland. From this core a sample from Opalinus Clay unit (Figures 6a and 6c) and Braun Dogger unit (Figures 6b and 6d) was broad ion beam polished and imaged in a SEM. In Figure 6 the image plane is perpendicular to bedding and the

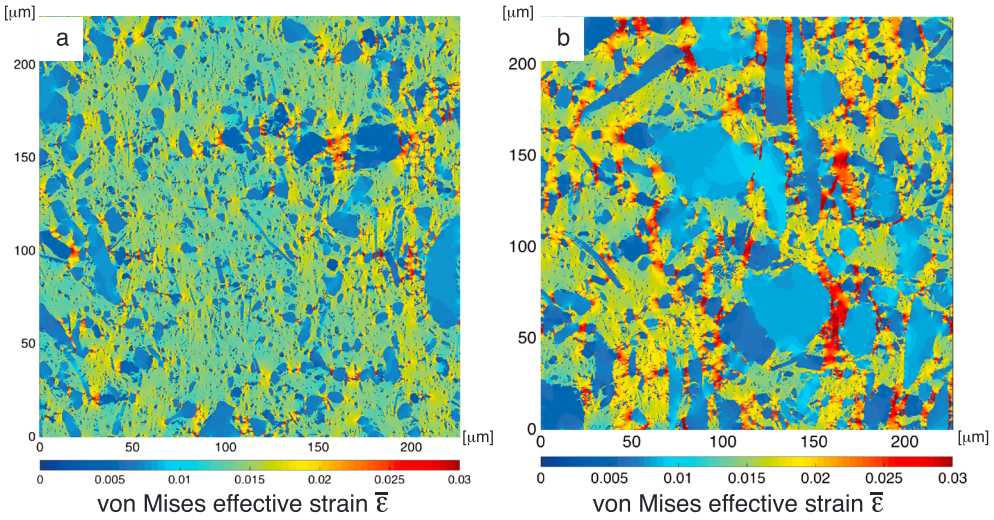

Figure 7. Von Mises effective strain maps showing the distribution of strain in case an external strain of $\varepsilon_x = \varepsilon_y = 0.01$ is applied to the microstructures depicted in Figure 6. (a) Sample from the Opalinus Clay unit with a high content of clay matrix. (b) Sample from the Braun Dogger unit with lower content of clay matrix. Note that blue colored minerals are mechanically strong nonclayey minerals.

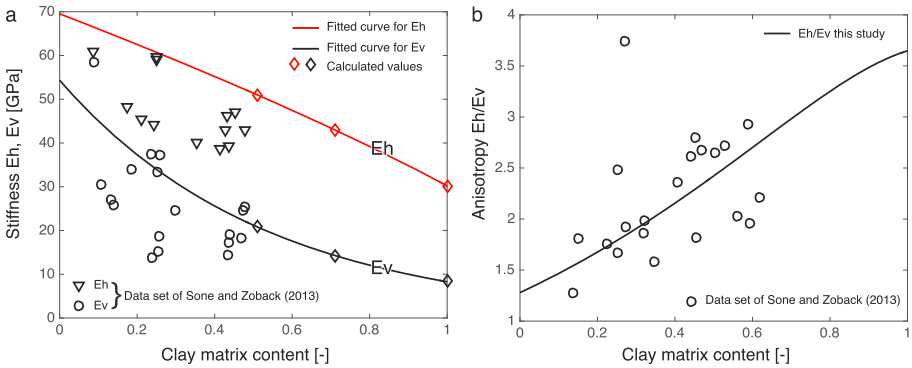

Figure 8. (a) Effects of clay matrix content on vertical (E_v) and horizontal (E_h) stiffness. Red and black diamonds are values, which were calculated using voxel-based finite element modeling in combination with microstructures depicted in Figure 6 and for a clay matrix content of 1. Red and black curves were fitted to the calculated values. Black triangles and circles are values in the data set of *Sone and Zoback* [2013]. (b) Black line is the ratio between horizontal and vertical stiffness obtained by dividing the fitted curves. Black circles are values in the data set of *Sone and Zoback* [2013].

difference in clay matrix content is well recognizable. The images were carefully segmented into major constituents and were then used as input for the elastic calculations. Because the elastic calculations were done on the base of 2-D SEM images (see above), we assumed plane strain conditions perpendicular to the bedding plane.

FEM simulations allowed constructing elastic strain maps, which give insights into local elastic deformation. Figure 7 shows the distribution of von Mises effective strain in case an external strain of $\varepsilon_x = \varepsilon_y = 0.01$ is applied to the microstructures depicted in Figure 6. As it can be expected, strain is higher within the mechanically weak fined-grained clay matrix when compared to strain in mechanically strong nonclayey mineral grains (Figure 7). Within the clay matrix, higher strain is localized along bottlenecks between nonclayey mineral grains. Thereby, strain localization is restricted to the bottlenecks, which are near parallel to bedding (vertical orientation in Figure 7). This effect is more pronounced in the sample with the low content of clay matrix (Figure 7b).

The actual goal of the FEM simulations is to calculate an effective **S**, which corresponds to the microstructure depicted in Figure 6. For details of the calculation procedure the reader is referred to the work of *Meille and Garboczi* [2001]. From the 2-D compliance matrix the effective stiffness perpendicular E_v and parallel E_h to bedding was calculated and plotted versus the clay matrix content (Figure 8). The calculations indicate a significant stiffness reduction with increasing clay matrix content (Figure 8a). By comparing the calculated values with data set of *Sone and Zoback* [2013], we find that our calculations predict a higher stiffness (Figure 8a). This can be explained in that the data set of *Sone and Zoback* [2013] is related to gas shales, which contain a not negligible amount of mechanically weak kerogen. With increasing clay matrix content the anisotropy E_h/E_v increases (Figure 8b). Furthermore, the calculations predict a low stiffness anisotropy even in the absence of a clay matrix. In the present case this low anisotropy is related to a preferred orientation of elongated nonclayey minerals (Figure 6). The predicted anisotropy E_h/E_v is in good agreement with the data set of *Sone and Zoback* [2013] (Figure 8b). This shows that the high experimentally determined microscale anisotropy of the porous clay matrix ($E_h/E_v = 3.75$) is realistic if not crucial if one wants to understand the measured anisotropy on the macroscale.

5. Conclusions

Microscale uniaxial compressive strength of the fine-grained porous clay matrix is substantially higher when compared to values obtained by macroscale strength testing. Differences in strength are likely related to differences in sample size, but differences in water saturation or differences in the experiential setup may also be reasons for the strength differences.

When a load is applied in direction parallel to bedding, failure is associated with the formation of multiple fractures with preferred fracture orientations near parallel to bedding. Multiple fracturing is not observed

when a load is applied in direction perpendicular to bedding. Hence, the orientation of the bedding relative to the load direction largely controls microfracturing.

Microscale stiffness is higher compared to macroscale stiffness, which can be explained by the presence of pores, preexisting cracks, and other flaws in larger specimens. In addition, microscale anisotropy E_h/E_v of the clay matrix is higher when compared to values obtained by marcoscale mechanical testing. An upscaling procedure shows that the measured high anisotropy of the fine-grained clay matrix is crucial to explain the observed macroscale anisotropy.

Acknowledgments
This work was funded by the Swiss National Cooperative for the Disposal of Radioactive Waste (NAGRA) as part of the SHARC consortium, a research collaboration between the Commonwealth Scientific and Industrial Research Organization (CSIRO), Curtin University of Technology, and NAGRA. The stress-strain data and the backscatter electron images, the latter of which were used in combination with finite element simulations, can both be accessed via https://drive.switch.ch/index.php/s/N5QLmvJasBlTcfu. The Fortran 77 source code used for voxel-based finite element modeling and the related manual is freely available at https://www.nist.gov/services-resources/software/finite-elementfinite-difference-programs. We would like to thank two anonymous reviewers for their suggestions and comments.

References

Abousleiman, Y. N., K. L. Hull, Y. Han, G. Al-Muntasheri, P. Hosemann, S. Parker, and C. B. Howard (2016), The granular and polymer composite nature of kerogen-rich shale, *Acta Geotech.*, *11*, 573–594.

Andra (2005), Dossier 2005 Argile: Evaluation de la faisabilité du stockage géologique en formation argileuse profonde—Rapport de synthèse. Juin 2005, Andra, France. [Available at <<http.//www. Andra.fr>>.]

Arns, C. H., M. A. Knackstedt, W. V. Pinczewski, and E. J. Garboczi (2002), Computation of linear elastic properties from microtomographic images: Methodology and agreement between theory and experiment, *Geophysics*, *67*, 1396–1405.

Ashby, M., and D. Jones (1980), *Engineering Materials*, Pergamon Press, Oxford.

Bobko, C. P., and F.-J. Ulm (2008), The nano-mechanical morphology of shale, *Mech. Mater.*, *40*(4), 318–337.

Del Viso, J. R., J. R. Carmona, and G. Ruiz (2008), Shape and size effect on the compressive strength of high-strength concrete, *Cem. Concr. Res.*, *38*, 386–395.

Garboczi, E. J. (1998), Finite element and finite difference programs for computing the linear electric and elastic properties of digital images of random materials, NIST.

Giger, S., P. Marschall (2014), Geomechnical properties, rock models and in-situ stress conditions for Opalinus Clay in Northern Switzerland. Arbeitsbericht NAB 14-01, Nagra Wettingen, Switzerland.

Griffith, A. A. (1921), The phenomena of rupture and flow in solid, *Philos. Trans. R. Soc. London, Ser. A*, *221*, 163–198.

Howie, P. R., S. Korte, and W. J. Clegg (2012), Fracture modes in micropillar compression of brittle crystals, *J. Mater. Res.*, *27*, 141–151.

Kanit, T., S. Forest, I. Gailliet, V. Mounoury, and D. Jeulin (2003), Determination of the representative volume for random composites: Statistical and numerical approach, *Int. J. Solids Struct.*, *40*, 3647–3679.

Keller, L. M., A. Hilger, and I. Manke (2015), Impact of sand content on solute diffusion in Opalinus Clay, *Appl. Clay Sci.*, *112-113*, 134–142.

Keller, L. M. (2016), Pore geometry effects on elastic properties of Opalinus Clay, *Geophyiscs*, *81*, D543–D551.

Love, A. E. H. (1927), *A Treatise on the Mathematical Theory of Elasticity*, 662 pp., Dover, New York.

Maeder, X., W. M. Mook, C. Niederberger, and J. Michler (2011), Quantitative stress/strain mapping during micropillar compression, *Philos. Mag.*, *91*(7), 1097–1107.

Madadi, M., A. C. Jones, C. H. Arns, and M. A. Knackstedt (2009), 3D imaging and simulation of elastic properties of porous materials, *Comput. Sci. Eng.*, *11*, 65–73.

Mavko, G., T. Mukerji, and J. Dvorkin (2009), *The Rock Physics Handbook: Tools for Seismic Analysis of Porous Media*, 511 pp., Cambridge Univ. Press, Cambridge, U. K.

Meille, S., and E. J. Garboczi (2001), Linear elastic properties of 2D and 3D models of porous materials made from elongated objects, *Modell. Simul. Mater. Sci. Eng.*, *9*, 371–390.

Michler, J., K. Wasmer, S. Meier, F. Östlund, and K. Leifer (2007), Plastic deformation of gallium arsenide micropillars under uniaxial compression at room temperature, *Appl. Phys. Lett.*, *90*(4) 043123.

Nagra (2002), Projekt Opalinuston—Synthese der geowissenschafftlichen Untersuchungsergebnisse. Entsorgungsnachweis für abgebrannte Brennelemente, verglaste hochaktive sowie langlebige mittelaktive Abfälle. Nagra Tech. Rep. NTB 02-03, Nagra Wettingen, Switzerland.

Nagra (2004), Effects of post-disposal gas generation in a repository for spent fuel, high-level waste and long-lives intermediate waste sited in the Opalinus Clay. Nagra Tech. Rep. NTB 04-06, Nagra, Wettingen, Switzerland.

Naumann, M., and I. Plischke (2005), Anisotropy of thermo-mechanical properties of Opalinus Clay—Heater experiment (HE), Deliverable 8c, WP3/Task 32, 50 p., Hannover (BGR).

Revil, A., and L. M. Cathles (1999), Permeability of shaly sands, *Water Resour. Res.*, *35*, 651–662, doi:10.1029/98WR02700.

Robinet, J.-C., P. Sardini, D. Coelho, J. C. Parneix, D. Prêt, E. Boller, and S. Altmann (2012), Effects of mineral distribution at mesoscopic scale on solute diffusion in a clay-rich rock example of the Callovo-Oxfordian mudstone (Bure, France), *Water Resour. Res.*, *48*, W05554, doi:10.1029/2011WR011352.

Sarout, J., and Y. Gueguen (2008), Anisotropy of elastic wave velocities in deformed shales. Part 1—Modeling results, *Geophysics*, *73*, D91–D103.

Schwiedrzik, J., R. Raghavan, A. Buerki, V. LeNader, U. Wolfram, J. Michler, and P. Zysset (2014), In situ micropillar compression reveals superior strength and ductility but an absence of damage in lamellar bone, *Nat. Mater.*, *13*(7), 740–747, doi:10.1038/NMAT3959.

Sone, H., and M. D. Zoback (2013), Mechanical properties of shale-gas reservoir rocks—Part 1: Static and dynamic elastic properties and anisotropy, *Geophysics*, *78*, D381–D392.

Soler, R., J. M. Molina-Aldareguia, J. Segurado, and J. LLorca (2012), Effect of misorientation on the compression of highly anisotropic single-crystal micropillars, *Adv. Eng. Mater.*, *14*, 1004–1008.

Soler, R., J. M. Wheeler, H.-J. Chang, J. Segurado, J. Michler, J. LLorca, and J. M. Molina-Aldareguia (2014), Understanding size effect on the strength of single crystals trough high-temperature micropillar compression, *Acta Mater.*, *81*, 50–57.

Ulm, F.-J., and Y. N. Abousleiman (2006), The nanogranular nature of shale, *Acta Geotech.*, *1*(2), 77–88.

Vanorio, T., M. Prasad, and A. Nur (2003), Elastic properties of dry clay mineral aggregates, suspensions and sandstones, *Geophys. J. Int.*, *155*, 319–326.

Veytskin, Y. B., V. K. Tammina, C. P. Bobko, P. G. Hartley, M. B. Clennell, D. N. Dewhurst, and R. R. Dagastine (2017), Micromechanical characterization of shales though nanoindenation and energy dispersive X-ray spectrometry, *Geomech. Energy Environ.*, *9*, 21–35.

Walsh, J. B. (1965), The effect of cracks on the uniaxial elastic compression of rocks, *J. Geophys. Res.*, *70*, 399–411, doi:10.1029/JZ070i002p00399.

Wenk, H.-R., M. Voltolini, M. Mazurek, L. R. Van Loon, and A. Vinsot (2008), Preferred orientation and anisotropy in shales: Callovo-Oxfordian shale (France) and Opalinus Clay (Switzerland), *Clays Clay Miner.*, *56*, 285–306.

Wheeler, J. M., C. Niederberger, C. Tessarek, S. Christiansen, and J. Michler (2013), Extraction of plasticity parameters of GaN with high temperature, in situ micro-compression, *Int. J. Plast.*, *40*, 140–151.

Zhang, H., B. E. Schuster, Q. Wei, and K. T. Ramesh (2006), The design of accurate micro-compression experiments, *Scripta Mater.*, *54*(2), 181–186.